

## Binary-optimization-based Multilayers and Their Practical Applications

**Geon-Tae Park<sup>1</sup>, Rira Kang<sup>2</sup>, Byunghong Lee<sup>2</sup>, and Sun-Kyung Kim<sup>1\*</sup>**

<sup>1</sup>*Department of Applied Physics, Kyung Hee University, Yongin 17104, Korea*

<sup>2</sup>*Energy Device Research Team, Advanced Vehicle Platform Division,  
Hyundai Motor Co., Uiwang 16082, Korea*

(Received October 31, 2024 : accepted November 11, 2024)

Multilayers composed of two or more materials enable the regulation of transmission, reflection, and absorption spectra across one or multiple bands. While analytic formulas based on well-established interference conditions, such as those employed in single-, double-, and triple-layer antireflective coatings and distributed Bragg reflectors, have provided suitable solutions for traditional optical coatings, they are limited in achieving the intricate spectral characteristics required by multifunctional optical coatings. To overcome this limitation, a variety of machine learning-based design algorithms have been rigorously studied. Among these, binary optimization has proven particularly effective for designing multilayer optical coatings. This approach transforms a given multilayer into a binary vector with multiple bits, where each bit represents one of the constituent materials, and quickly identifies an optimal figure-of-merit by analyzing the interactions among the elements of the binary vector. In this review article, we elucidate the principles of binary optimization and explore its applications in the design of multilayers for antireflective coatings for high-numerical-aperture lenses, transparent radiative coolers for energy-saving windows, and bandpass filters for thermophotovoltaics. Furthermore, we address the limitations, challenges, and perspectives of machine learning-based optical design to guide directions for future research in this field.

**Keywords :** Binary optimization, Machine learning, Multilayer, Optical coating, Optical design

**OCIS codes :** (200.0200) Optics in computing; (220.0220) Optical design and fabrication; (310.0310) Thin films; (310.1210) Antireflection coatings; (310.6845) Thin film devices and applications

### I. INTRODUCTION

Multilayer optical coatings are constructed by stacking dielectric and/or metallic layers with subwavelength thicknesses [1]. These multilayers are prevalent in everyday applications due to their capacity to precisely regulate light transmission, reflection, and absorption over specific or broad wavelengths [2]. This ability facilitates the creation of antireflective and antiglare coatings [3–6], mirrors, and spectral filters [7–10], which are integral to the functional-

ity of solar cells [11–15], windows [16–20], lasers [21–23], and display technologies [24–27]. Analytical formulas such as single-, double-, and triple-layer configurations are often employed to design antireflective coatings (ARCs) [28, 29]. These formulas are used by selecting the appropriate configuration based on the availability of materials, specifically their refractive indices, along with the desired bandwidth and economic considerations. Similarly, distributed Bragg reflectors (DBRs) are designed using an analytical approach [30]; They consist of multiple layers of alternating

\*Corresponding author: sunkim@khu.ac.kr, ORCID 0000-0002-0715-0066

Color versions of one or more of the figures in this paper are available online.



This is an Open Access article distributed under the terms of the Creative Commons Attribution Non-Commercial License (<http://creativecommons.org/licenses/by-nc/4.0/>) which permits unrestricted non-commercial use, distribution, and reproduction in any medium, provided the original work is properly cited.

Copyright © 2024 Current Optics and Photonics

materials with high and low refractive indices, where each repeated pair has a quarter-wave thickness. These examples illustrate the application of well-defined destructive or constructive interference for managing partial reflective waves.

Although analytical formulas provide exact solutions for straightforward optical designs, they are constrained to perform multispectral engineering or to generate stepwise spectral profiles, both of which necessitate a greater complexity of variables. Multispectral engineering entails the independent regulation of light transmission, reflection, and absorption across multiple spectral bands or within the wavelength-incident angle domain, thus presenting a formidable challenge from the perspective of classical approaches. For example, transparent radiative coolers (TRCs) designed for energy-saving windows must concurrently achieve high transmittance in the visible (400–700 nm), high reflectance in the near-infrared (700–2,500 nm), and high emissivity (characterized by absorption according to Kirchhoff's law of thermal radiation) in the mid-infrared (8–14  $\mu\text{m}$ ) [31]. Likewise, stepwise spectral profiles are crucial for applications such as cooling windows [32], photon recycling in incandescent lighting [33], and near-infrared cutoff filters for complementary metal-oxide-semiconductor image sensors [34]. Although DBRs provide complete reflection within a photonic bandgap, they exhibit residual reflectance outside the bandgap, which undermines the creation of a stepwise spectrum. Moreover, challenges such as the lack of materials with desired refractive indices, in addition to considerations of fabrication tolerance and cost-effectiveness (*e.g.*, the number of interfaces and total thickness), complicate the application of existing analytical formulas.

To address these limitations, various inverse design methods based on machine learning have been developed and employed, including needle optimization [35–38], memetic algorithm [39–41], genetic algorithm [42–47], neural networks [48–50], and reinforcement learning [51, 52]. It is well known that binary optimization is particularly effective for designing multilayer optical coatings [53]. This approach converts a given multilayer into a binary vector composed of multiple bits, where each bit corresponds to one of the constituent materials with a required thickness, typically one-tenth of an operational wavelength. It examines the interactions among the elements of the binary vector and swiftly identifies an optimal (or minimal) figure-of-merit (FoM) using sampling methods such as brute force (BF), simulated annealing (SA), and quantum annealing (QA). BF evaluates every possible solution within the parameter space, ensuring the identification of the global optimum in a given machine learning model. However, it is computationally expensive and impractical for large-scale problems with extensive parameter spaces. SA offers a probabilistic technique that explores the solution space by allowing occasional uphill moves, thus circumventing local minima. While more computationally efficient than BF, it may still require significant computational resources and

careful tuning of its parameters to balance exploration and exploitation. QA promises faster convergence for certain problem classes, particularly those with intricate energy landscapes. However, its practical application is limited by current technological constraints (*i.e.*, the availability of quantum bits). The selection of a sampling method depends on the specific problem characteristics, including the size and complexity of the parameter space, computational resources, and the required tolerance of the solution. In principle, binary optimization can reveal multiple multilayer configurations that achieve similar levels of FoM within an acceptable tolerance, thereby facilitating the selection of a more economically viable solution. For instance, minimizing the number of interfaces, the variety of materials employed, and the overall thickness can serve as guidelines for determining the optimal endpoint among multiple multilayer solutions.

In this review article, we elucidate the principles of binary optimization and investigate its applications in designing multilayers for ARCs [54, 55], TRCs for energy-saving windows [56], and bandpass filters for thermophotovoltaics (TPVs) [57, 58]. In addition, we discuss the limitations, challenges, and perspectives of machine learning-based optical design, thereby indicating potential directions for future research in this field.

## II. PRINCIPLES AND APPLICATION OF BINARY OPTIMIZATION

### 2.1. Binary-optimization-based Multilayers Design

Recently, the use of machine learning to design optical structures has gained immense popularity. As the demand for complex optical specifications such as broad spectrum, wide incident angles, and multispectral objectives, continues to rise, traditional analytical solutions became inadequate. Addressing these complex problems often requires non-intuitive designs, which can be successfully discovered using machine learning due to its ability to explore extensive parametric spaces within a limited computational timeframe [35–58]. For a machine learning-based approach to be effective, it is crucial to select an optimization method that strikes a balance between accuracy and computational cost. In this regard, binary-optimization-based multilayer design offers a robust optimization framework by compressing the dimensionality of the system into a simplified binary representation [53].

The binary-optimization-based multilayer design involves four main steps [Fig. 1(a)].

#### 2.1.1. Encoding the Multilayer

The first step is to encode the multilayer into a binary vector. This process transforms the continuous system into finite  $N$  dimensions representing both refractive indices and thicknesses as binary digits. This discretization is essential for mapping the physical problem into a quadratic unconstrained binary optimization (QUBO) problem, a common

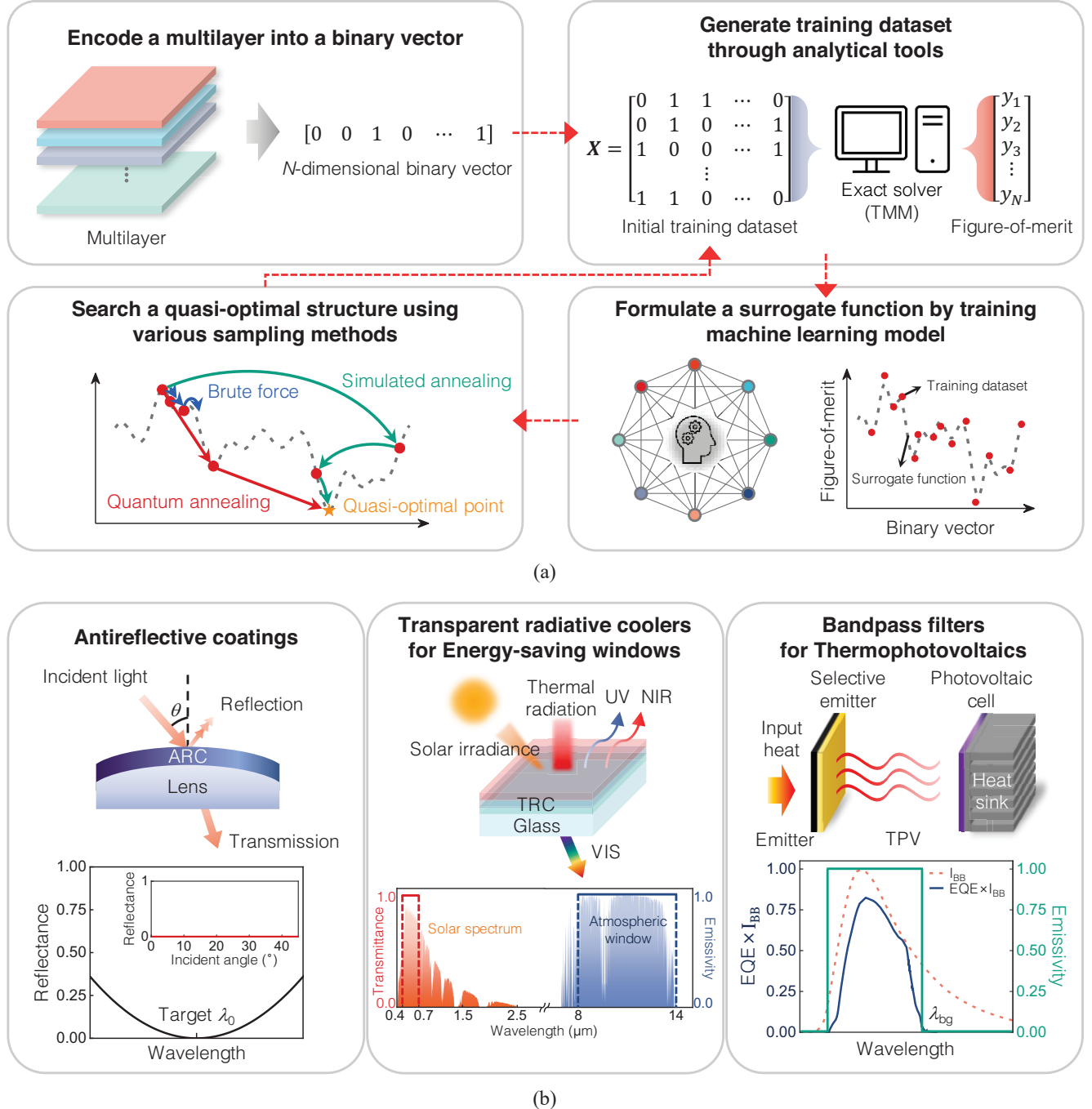


**FIG. 1.** Workflow of binary-optimization-based multilayer design and its applications. (a) Schematic of the iterative optimization cycle, composed of four primary steps [53]. (b) (i) Schematic of antireflective coatings (ARC) applied to a lens, designed to minimize reflectance at the target wavelength  $\lambda_0$  over a wide range of incident angles  $\theta$ . (ii) Illustration of transparent radiative coolers (TRCs) for energy-saving windows, engineered to reflect ultraviolet and near-infrared light while transmitting visible light, and maintaining high emissivity within the atmospheric window. The red line represents the target transmittance spectrum, and the blue line represents the target emissivity spectrum for an ideal transparent radiative cooler. (iii) Schematic of bandpass filters for thermophotovoltaics (TPVs), designed to enhance the efficiency of the photovoltaic (PV) cell by selective emission. The red dashed line represents the spectral irradiance of a blackbody  $I_{BB}$ , and the blue solid line represents the external quantum efficiency (EQE) multiplied by the intensity of blackbody radiation ( $I_{BB}$ ). The green solid line shows the target spectrum of a selective emitter with unit emissivity.

and versatile approach for addressing various optical systems and combinatorial optimizations.

### 2.1.2. Generating the Initial Training Dataset

The second step involves generating the initial training dataset, represented as a binary vector. An exact solver such as the transfer matrix method (TMM) yields the

FoM, providing an accurate initial dataset for training the machine learning model. The FoM can represent various optical properties, including transmittance, reflectance, or emissivity, and can account for complex conditions such as wide-angle performance or multispectral requirements. This versatility highlights a key advantage of the binary-optimization-based method, allowing users to define any objective function by specifying the FoM equation.

### 2.1.3. Formulating a Surrogate Function

The third step involves creating a surrogate function, a predictive model that approximates the FoM without requiring detailed internal analysis of the interactions of elements in a multilayer, which significantly reduces computational demands. There are various models capable of optimizing the QUBO problem, such as factorization machines (FM) and Bayesian optimization. The choice of an appropriate machine learning model depends on the complexity of the optimization problem. For example, FM is advantageous for sparse initial data, making it suitable for smaller parametric spaces.

### 2.1.4. Searching a Quasi-optimal Point

The final step is searching for a quasi-optimal structure among the configurations evaluated by the surrogate function. The selection of a suitable sampling method is critical to efficiently identify the optimal point. BF evaluates all possible FoM values but requires extensive computational resources, while methods such as SA and QA use probabilistic approaches to approximate the quasi-optimal solution. Probabilistic methods are especially effective for large datasets and limited computational resources, as they enable significant advances during the search process and accelerate optimization. After identifying the quasi-optimal point, the corresponding binary vector and FoM value are fed back into the training dataset, and the optimization process is iterated until convergence on the desired point.

This methodology finds application in ARCs for high-numerical-aperture lenses, TRCs for energy-saving windows, and bandpass filters for TPVs [Fig. 1(b)] [54–58]. In the semiconductor fabrication and inspection industries, high-numerical-aperture lenses are in demand to ensure superior resolution [59, 60]. Binary-optimization-based multilayer design identifies ARC structures with minimal reflectance over a wide range of incident angles, which is essential for high-numerical-aperture lenses operating at a target wavelength ( $\lambda_0$ ) [54, 55]. Another application is TRCs for energy-saving windows, driven by the need to effectively manage the thermal properties of buildings and vehicles. TRCs aim to provide high transmittance in the visible spectrum, high reflectance in the ultraviolet (UV) and near-infrared (NIR) regions, and high emissivity in the mid-infrared range (8–14  $\mu\text{m}$ ). Given the multispectral and multi-objective requirements, machine learning-based optimization is advantageous for designing TRCs [56]. The third application is bandpass filters for TPVs. Bandpass

filters act as selective emitters in TPV systems and significantly enhance photon absorption efficiency in photovoltaic (PV) cells. To reject non-useful photons, a bandpass filter must achieve unit emissivity within the bandwidth corresponding to maximum external quantum efficiency (EQE) of the PV cell. Hence, a machine learning approach allows for customization of bandpass filters to meet the target emissivity spectrum and enhance photon absorption for various PV cell types [57, 58].

## 2.2. ARCs for High-numerical-aperture Lenses

In the semiconductor inspection and lithography sector, high-numerical-aperture lenses for short-wavelength lasers such as ArF (193 nm) and KrF (248 nm) are essential for achieving superior resolution [61–66]. It remains challenging to design ARCs with angle-independent antireflective performance for deep-ultraviolet (DUV) wavelengths (190–350 nm). A major issue is the limited selection of transparent DUV materials, which are primarily fluoride and oxide-based dielectrics such as  $\text{CaF}_2$ ,  $\text{MgF}_2$ ,  $\text{LaF}_3$ ,  $\text{AlF}_3$ , and  $\text{Al}_2\text{O}_3$  [67–71]. These dielectrics offer a narrow range of refractive indices, which restricts design flexibility. In addition, the requirement for ultrathin films with minimal interfaces to mitigate fabrication-induced stress adds another layer of complexity to the design of DUV ARCs. Furthermore, high-numerical-aperture lenses require ARCs that perform effectively over a broad range of incident angles, but it is difficult to achieve omnidirectional antireflection in the absence of well-established analytical formulas.

To address these challenges, Kim *et al.* [54] proposed a binary-optimization-based multilayer design approach for DUV ARCs with FM as a machine learning model [72] and BF as a sampling method. Figure 2(a) illustrates a schematic with the FoM equation and the building blocks for producing ARCs. The multilayers are designed to minimize the average reflectance of both *s*-polarized and *p*-polarized light across wide incident angles ( $0^\circ$  to  $45^\circ$ ) at a wavelength of 193 nm. For transparent DUV materials,  $\text{MgF}_2$  and  $\text{LaF}_3$  are encoded as 0 and 1, respectively. Each bit represents a thickness of 10 nm, and  $\text{CaF}_2$  is chosen as a substrate material. The structure depicted in Fig. 2(a) can be represented as a binary vector  $\{0\ 1\ 1\ 0\ 0\ 0\ 1\ 1\}$  from the top layer, with 8 bits ( $N_{\text{bit}}$ ) and four physical layers ( $N_{\text{layer}}$ ). The design process involves two stages: Discrete optimization (DO) using FM and continuous optimization (CO) using the interior-point (IP) method, as shown in Fig. 2(b). Given the constant bit thickness of 10 nm, FM explores the parametric space in discrete, larger steps. After this initial optimization, the thicknesses of the continuous layers are further refined using the IP method with a resolution of 1 nm. This finer adjustment moves the solution closer to the quasi-optimum point, reducing the risk of being trapped in local minima. Figure 2(c) presents the simulation results for both one-step (DO only) and two-step (DO followed by CO) optimizations as  $N_{\text{bit}}$  increases. The top panel in Fig. 2(c) displays the trend of the log-scaled FoM values.

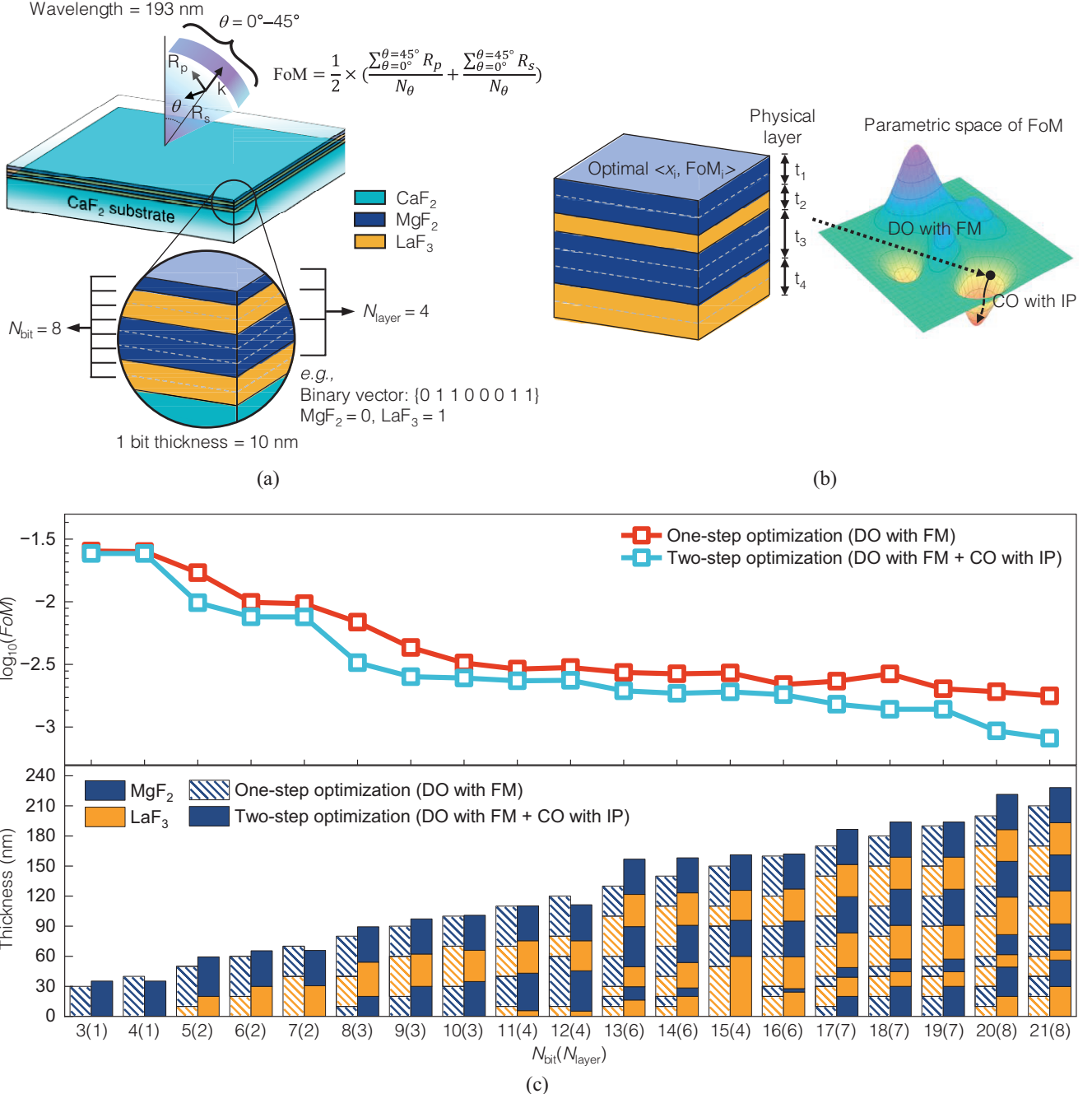


**FIG. 2.** Simulated results and experimental analysis of deep ultraviolet antireflective coatings (DUV ARCs). (a) Schematic illustrating the complexity of designing DUV ARCs. The figure-of-merit (FoM) is defined as the average reflectance across incident angles from  $0^\circ$  to  $45^\circ$  at a wavelength of 193 nm. The ARC consists of alternating layers of  $\text{AlF}_3$  and  $\text{Al}_2\text{O}_3$ , with each bit set to a thickness of 10 nm, deposited on a  $\text{CaF}_2$  substrate. (b) Schematics of the two-step optimization process used in designing the DUV ARC. Continuous optimization (CO) combined with IP refines the thickness of physical layers that were initially optimized using discrete optimization (DO) with factorization machines (FM). (c) Simulated FoM values (top) comparing one-step optimization (DO with FM) (red line) and two-step optimization (CO with IP) (blue line). The corresponding material composition and layer thicknesses (bottom) are shown for various  $N_{\text{bit}}(N_{\text{layer}})$  values. (d) Simulated reflectance spectra over a broad range of wavelengths (180–300 nm) and incident angles ( $0^\circ$ – $45^\circ$ ) for the various optimized structures. (e), (f) Simulated and measured reflectance values for incident angles of  $0^\circ$  (e) and  $45^\circ$  (f) at a wavelength of 193 nm. The insets show the simulated and measured reflectance spectra for the structure with  $N_{\text{bit}}(N_{\text{layer}}) = 10(3)$ . Adapted and modified from Kim *et al.*, Nanophotonics 2023; **12**; 1913–1921. Copyright © 2023, Kim *et al.* [54] (continued).

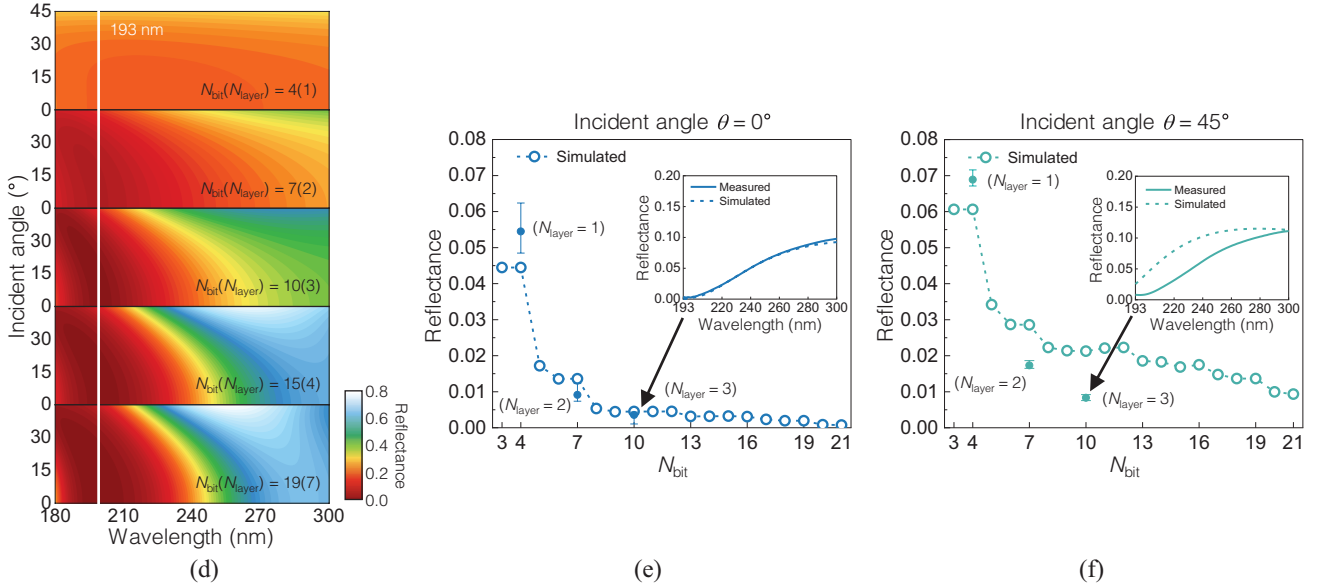


**FIG. 2.** Simulated results and experimental analysis of deep ultraviolet antireflective coatings (DUV ARCs). (a) Schematic illustrating the complexity of designing DUV ARCs. The figure-of-merit (FoM) is defined as the average reflectance across incident angles from  $0^\circ$  to  $45^\circ$  at a wavelength of 193 nm. The ARC consists of alternating layers of  $\text{AlF}_3$  and  $\text{Al}_2\text{O}_3$ , with each bit set to a thickness of 10 nm, deposited on a  $\text{CaF}_2$  substrate. (b) Schematics of the two-step optimization process used in designing the DUV ARC. Continuous optimization (CO) combined with IP refines the thickness of physical layers that were initially optimized using discrete optimization (DO) with factorization machines (FM). (c) Simulated FoM values (top) comparing one-step optimization (DO with FM) (red line) and two-step optimization (CO with IP) (blue line). The corresponding material composition and layer thicknesses (bottom) are shown for various  $N_{\text{bit}}(N_{\text{layer}})$  values. (d) Simulated reflectance spectra over a broad range of wavelengths (180–300 nm) and incident angles ( $0^\circ$ – $45^\circ$ ) for the various optimized structures. (e), (f) Simulated and measured reflectance values for incident angles of  $0^\circ$  (e) and  $45^\circ$  (f) at a wavelength of 193 nm. The insets show the simulated and measured reflectance spectra for the structure with  $N_{\text{bit}}(N_{\text{layer}}) = 10(3)$ . Adapted and modified from Kim *et al.*, Nanophotonics 2023; **12**; 1913–1921. Copyright © 2023, Kim *et al.* [54].

The red and blue lines correspond to the one-step and two-step optimizations, respectively. As  $N_{\text{bit}}$  increases, the FoM, which is an average angular reflectance, decreases in both cases. Specifically, at  $N_{\text{bit}}$  values of 3 and 10, the one-step optimization results in FoMs of 0.025 and 0.003, while the two-step optimization achieves slightly lower values of 0.024 and 0.002. The FoM values remain marginally changed for  $N_{\text{bit}}$  from 10 to 19, decrease slightly to 0.0009 at  $N_{\text{bit}} = 20$ , and reach a minimum value of 0.0008 at  $N_{\text{bit}} = 21$ . The two-step optimization consistently exhibits a slight improvement over the one-step optimization for all  $N_{\text{bit}}$  values. These findings indicate that DO with FM effectively explores the vast parametric space and provides a strong starting point close to the optimal solution.

The bottom panel of Fig. 2(c) illustrates the structure of the optimized ARCs. The topmost layer is consistently identified as  $\text{MgF}_2$ , a low refractive index material chosen to minimize reflectance at the air interface. As  $N_{\text{bit}}$  increases, the configurations of the multilayers become increasingly intricate, even though the number of physical layers does not directly scale with  $N_{\text{bit}}$ . For example, a multilayer optimized through two-step optimization at  $N_{\text{bit}}(N_{\text{layer}}) = 15(4)$  yields a simple four-layer configuration. This emphasizes the need to balance achieving a low FoM with maintaining fabrication fidelity, aiming for designs that provide similar FoM within an acceptable tolerance without unnecessarily

increasing the number of layers. Figure 2(d) shows the reflectance of multilayers optimized at  $N_{\text{bit}}$  values of 4, 7, 10, 15, and 19 as a function of the incident angle ( $0^\circ$ – $45^\circ$ ) and the wavelength (180–300 nm). Notably, structures with  $N_{\text{bit}}$  values of 10, 15, and 19 demonstrate superior antireflective performance across a wide range of incident angles and wavelengths (180–200 nm), indicating robustness in fabrication tolerance regarding thickness variations.

After the optimization process, experimental validation is performed. Figures 2(e) and 2(f) present the measured reflectance values at incident angles of  $0^\circ$  and  $45^\circ$  for fabricated samples with  $N_{\text{bit}}(N_{\text{layer}})$  values of 4(1), 7(2), and 10(3), along with the simulated results, which cover the entire range from  $N_{\text{bit}} = 3$  to 21. For both incident angles, reflectance significantly decreases as  $N_{\text{bit}}$  increased, which is consistent with the simulation trends shown in Fig. 2(c). At normal incidence, the sample with  $N_{\text{bit}}(N_{\text{layer}}) = 10(3)$  demonstrates the lowest reflectance, approximately 0.35%. For the  $45^\circ$  incident angle, the same sample shows a reflectance of approximately 0.8%. The insets in Figs. 2(e) and 2(f) highlight the good agreement between the experimental and simulated spectra.

Another study by Park *et al.* [55] focused on designing DUV ARCs for a KrF laser wavelength (248 nm) using FM, and additionally provided analysis for comparisons to analytically designed ARCs. The initial simulation setup

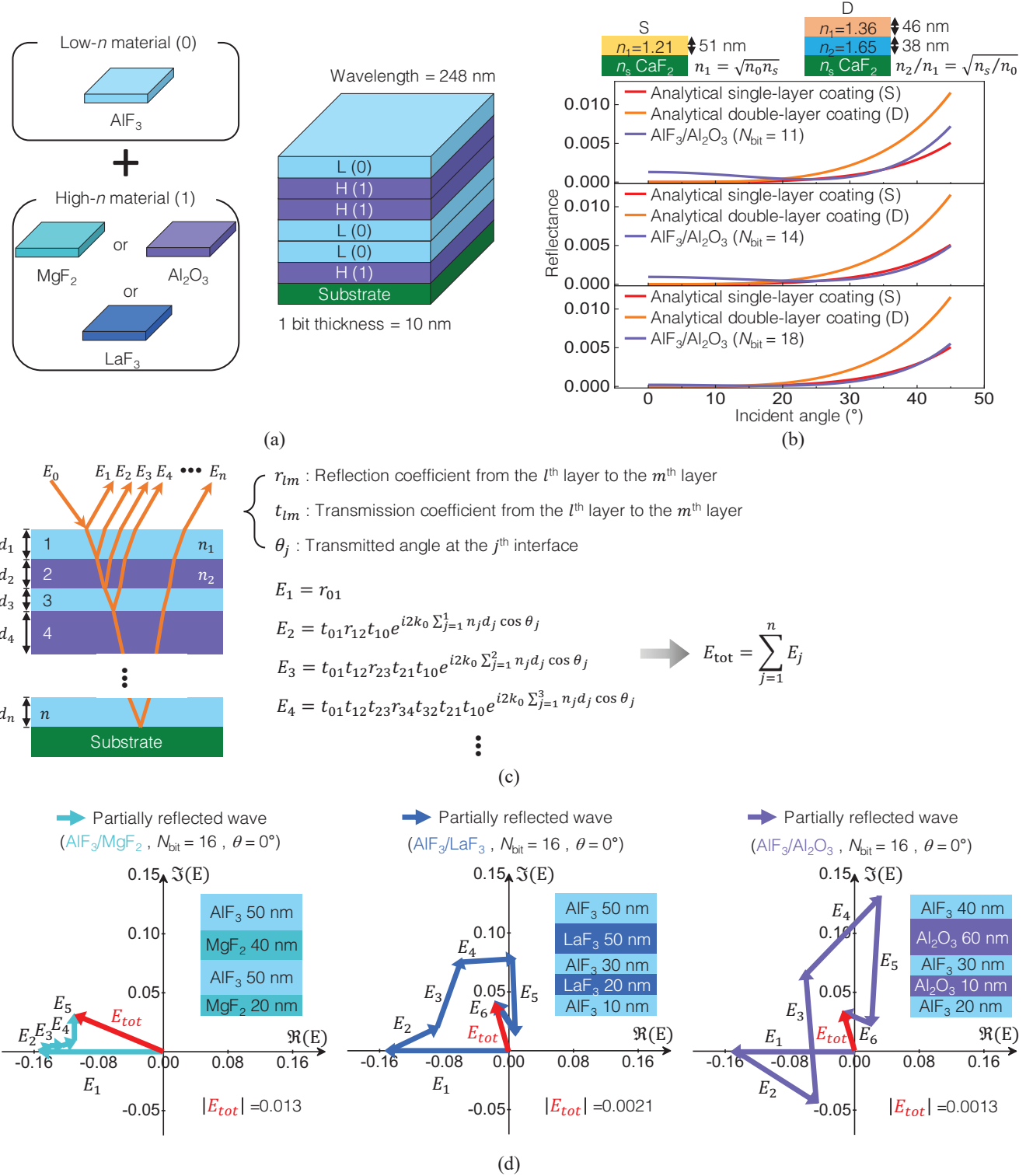


**FIG. 3.** Comparative analysis of angular reflectance spectra and phasor diagrams for deep ultraviolet antireflective coating (DUV ARC). (a) Schematic showing material compositions established as the basis for optimizing the DUV ARC at a wavelength of 248 nm. The material composition of the ARC consists of a combinatorial set of binary materials, with each bit thickness set as 10 nm. The low- $n$  material  $\text{AlF}_3$  is paired with high- $n$  material options,  $\text{MgF}_2$ ,  $\text{LaF}_3$ , and  $\text{Al}_2\text{O}_3$ . (b) Comparative analysis of angular reflectance for analytical single- and double-layer coatings along with the optimized  $\text{AlF}_3/\text{Al}_2\text{O}_3$  multilayer with three different  $N_{\text{bit}}$  values. (c) Schematic illustrating partially reflected waves as complex phasors, where the total reflectance of the multilayer can be approximated by the vector sum of these complex phasors. (d) Phasor diagrams for optimized ARCs with three different material combinations ( $\text{AlF}_3/\text{MgF}_2$ ,  $\text{AlF}_3/\text{LaF}_3$ , and  $\text{AlF}_3/\text{Al}_2\text{O}_3$ ) with  $N_{\text{bit}} = 16$  at normal incidence. Adapted and modified from Park *et al.*, Adv. Opt. Mater. 2024; **12**; 2401040. Copyright © 2024, with permission from Wiley-VCH GmbH [55].

involves a binary combination of materials consisting of a low-refractive-index (low- $n$ ) material, AlF<sub>3</sub> ( $n = 1.36$ ), paired with one of high-refractive-index (high- $n$ ) materials: MgF<sub>2</sub> ( $n = 1.40$ ), LaF<sub>3</sub> ( $n = 1.55$ ), or Al<sub>2</sub>O<sub>3</sub> ( $n = 1.71$ ) [Fig. 3(a)]. The low- $n$  material is encoded as “0” and the high- $n$  material as “1.” Each bit represents a thickness of 10 nm, and CaF<sub>2</sub> is used as a substrate material. A pair with the highest refractive index contrast, AlF<sub>3</sub>/Al<sub>2</sub>O<sub>3</sub>, shows the most effective antireflective performance. To highlight the performance of optimized AlF<sub>3</sub>/Al<sub>2</sub>O<sub>3</sub> multilayers, they are assessed against ARCs designed using analytical formulas based on quarter-wave thicknesses [Fig. 3(b)]. The reflectance of the optimized multilayer with  $N_{\text{bit}} = 18$  remains below 0.005 for incident angles between 0° and 45°. The observation of minimum reflectance around an incident angle of 23° for all configurations indicates that the machine learning aims to minimize the average reflectance across the considered angular range, rather than focusing solely on specific incident angles. Simulation results indicate that each optimized AlF<sub>3</sub>/Al<sub>2</sub>O<sub>3</sub> multilayer outperforms the analytical double-layer coating across all  $N_{\text{bit}}$  values. Notably, the AlF<sub>3</sub>/Al<sub>2</sub>O<sub>3</sub> multilayer at  $N_{\text{bit}} = 18$  achieves a FoM of 0.00094, which is almost identical to the FoM of 0.00096 from the analytical single-layer coating; the latter requires an extremely low refractive index ( $n = 1.21$ ), which is challenging to achieve in practice.

Phasor analysis is conducted to gain a deeper understanding of the underlying physical mechanisms of the designed ARCs [73–75]. Figure 3(c) provides a schematic representation of how partially reflected waves can be interpreted as phasors. The complex reflection and transmission amplitudes are obtained using Fresnel coefficients, where  $r_{lm}$  and  $t_{lm}$  represent reflection and transmission coefficients between layers  $l$  and  $m$ , respectively. The phase shifts are calculated from the optical path differences, which relies on the transmitted angle  $\theta_j$ , layer thickness  $d_j$ , and wave vector  $k_0$ .  $E_j$  represents the phasor from a first-order reflection wave at the  $j^{\text{th}}$  interface, ignoring higher-order reflections involving multiple reflections. The squared magnitude of the sum of all partial phasors ( $E_{\text{tot}}$ ) is then used to estimate the reflectance of the multilayer, and antireflective performance is evaluated by assessing how close  $E_{\text{tot}}$  converges to the origin. Phasor diagrams for the AlF<sub>3</sub>/MgF<sub>2</sub>, AlF<sub>3</sub>/LaF<sub>3</sub>, and AlF<sub>3</sub>/Al<sub>2</sub>O<sub>3</sub> multilayers at  $N_{\text{bit}} = 16$  under normal incidence are obtained [Fig. 3(d)]. The final phasor for the AlF<sub>3</sub>/MgF<sub>2</sub> multilayer diverges significantly from the origin with a relatively high  $E_{\text{tot}}$  value of 0.013, indicating its sub-optimal antireflective performance. In contrast, the AlF<sub>3</sub>/Al<sub>2</sub>O<sub>3</sub> multilayer exhibits a much lower  $E_{\text{tot}}$  value of 0.0013, which is an order of magnitude smaller, demonstrating its superior antireflective performance. The improvement can be attributed to the larger refractive index contrast between the binary materials, which increases the magnitudes of individual phasors and facilitates the convergence of  $E_{\text{tot}}$  toward the origin. Conversely, when the magnitudes of individual phasors are too small, the overall phasor sum

remains distant from the origin, with  $E_1$  being the dominant phasor.

### 2.3. TRCs for Energy-saving Windows

TRCs can be used as window coatings to reduce cooling energy requirements for buildings and vehicles, thus contributing significantly to mitigating climate change [31]. Currently, the energy used for cooling accounts for approximately 15% of total global energy consumption [76, 77]. Passive radiative coolers, which operate without external energy by dissipating heat into the cold outer space through the atmospheric window, have attracted much interest [78–86]. TRCs are designed to minimize optical heating by reflecting UV and NIR light (comprising ~50% of solar irradiance) while allowing high transmittance in the visible spectrum. In the mid-infrared range, which corresponds to the atmospheric window, TRCs require near-unity emissivity to maximize radiative cooling efficiency. Additionally, another recent study has focused on tuning visible transmittance to create customizable windows that adapt to user needs and different lighting conditions [87]. The main challenges in TRC design include the complexity of multispectral requirements and the limited availability of materials with negligible absorption across the solar spectrum. These types of multispectral, multi-objective design problems are beyond the capability of analytical methods and instead require machine learning-based optimization approaches.

Kim *et al.* [56] proposed a TRC design using FM as the machine learning model, with QA selected as the sampling method. QA, a quantum computing technique, is well-suited for optimizing all potential input combinations since qubits can evaluate the objective function instantaneously to find the minimum point and bypassing local minima [88–90]. Compared to exhaustive enumeration, which guarantees finding the global minimum but can be computationally expensive, the QA-assisted optimization is significantly faster, particularly for structures with high-level complexity. The TRC layer is positioned between the top polydimethylsiloxane (PDMS) layer and a glass substrate, which do not participate in the optimization process [Fig. 4(a)]. The TRC design employs quaternary bases (SiO<sub>2</sub> = 00, Si<sub>3</sub>N<sub>4</sub> = 01, Al<sub>2</sub>O<sub>3</sub> = 10, TiO<sub>2</sub> = 11) defined by combinations of binary digits, enabling the use of materials more than two within the binary-optimization framework. The structure is divided into  $N_{\text{bit}}$  layers with a total thickness of  $t_{\text{tot}} = 1,200$  nm, and each layer has a uniform thickness of  $t_{\text{tot}}/N_{\text{bit}}$ . The optimization is conducted for  $N_{\text{bit}}$  values of 8, 10, 12, 16, 20, and 24 to identify the optimal structure. As observed in the ARC case, TRC multilayers with larger  $N_{\text{bit}}$  values exhibit a tailored spectrum closer to the ideal spectrum due to the increased degrees of freedom. Figure 4(b) compares the best-performing structure at  $N_{\text{bit}} = 24$  with the ideal spectrum. The ideal transmittance spectrum is unity in the visible region and zero elsewhere, and is represented by the red line. For the transmittance spectrum of the optimal multilayer, the deviation from the ideal spectrum is notable

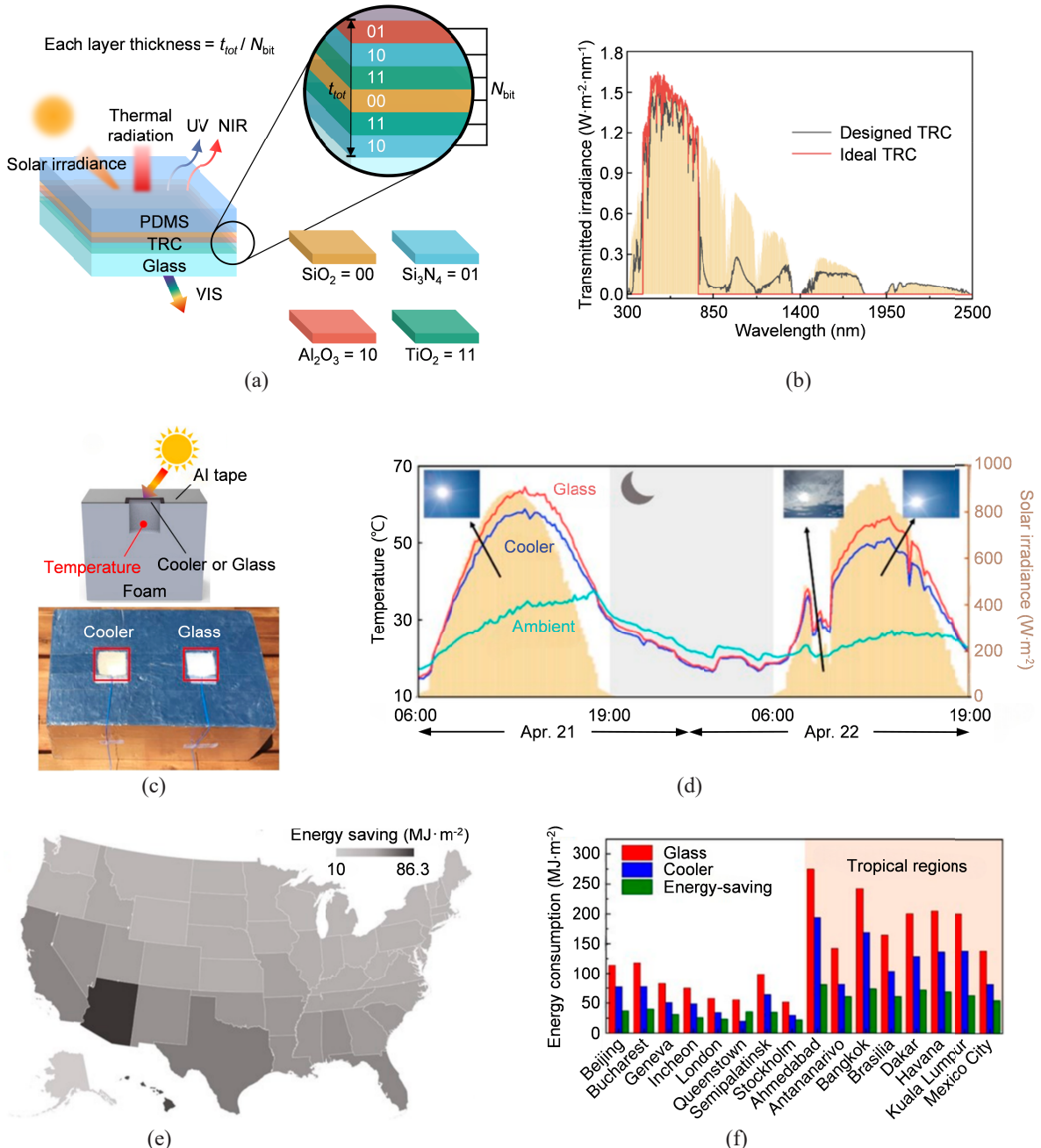


**FIG. 4.** Transparent radiative cooler (TRC) concept and experimental demonstrations. (a) Schematic illustrating the TRC as a planar multilayer deposited on a glass substrate with a polydimethylsiloxane (PDMS) top layer. Four materials ( $\text{SiO}_2$ ,  $\text{Si}_3\text{N}_4$ ,  $\text{Al}_2\text{O}_3$ , and  $\text{TiO}_2$ ) are selected to make the TRC. The thickness of each layer is calculated by dividing the total thickness by the number of layers. (b) Comparison of transmitted irradiance between the ideal and quantum annealing (QA)-designed TRC ( $N_{\text{bit}} = 24$ ). The yellow shaded region represents the solar spectral irradiance. (c) Schematic and photograph of the experimental setup simulating an insulated environment with a window, comparing the chamber temperatures when the designed TRC or reference glass is attached. (d) Measured temperatures of the two chambers over time, recorded during sunny days in Phoenix, AZ, USA, from 06:00 on April 21, 2022, to 19:00 on April 22, 2022. (e) Predicted cooling energy savings when the designed TRC is used as a window across the United States. The USA map is generated using Microsoft Excel (powered by Bing. @DSAT for MSFT, GeoNames, Navteq). (f) Energy consumption comparison in 16 cities worldwide between standard glass, a cooler, and the TRC-deposited energy-saving window. Adapted and modified from Kim *et al.*, ACS Energy Lett. 2022; 7: 4134–4141. Copyright © 2022, with permission from American Chemical Society [56].

for wavelengths greater than 1,400 nm. This discrepancy arises because the intensity of sunlight in the spectral region is much lower than in others, leading the machine learning model to prioritize matching the ideal spectrum in the vis-

ible. For experimental validation, the  $N_{\text{bit}} = 24$  multilayer (10 physical layers) is fabricated using thin-film vacuum deposition and tested in a thermally insulated chamber with the TRC on the top side next to a reference glass panel

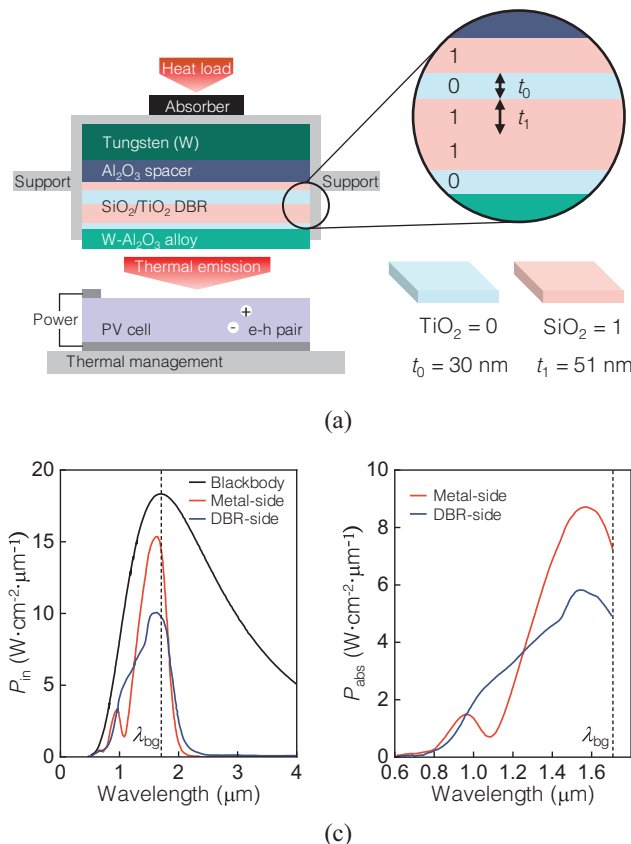
[Fig. 4(c)]. The sample is tested in Phoenix, CA, USA for 37 hours, and shows that the chamber with the TRC maintains a temperature up to 6.1 °C lower than the chamber with the glass panel [Fig. 4(d)]. In both chambers, the measured temperature is higher than the ambient temperature due to the visible transparency of the TRC, which allows solar heating. The annual energy savings for a standard office with the two windows in the USA is estimated using EnergyPlus™ software (National renewable energy laboratory, CO, USA). The average annual energy savings in the surveyed USA cities is 50 MJ·m<sup>-2</sup> when the TRC is used as a window coating [Fig. 4(e)]. In cities with hot and dry climates, such as Phoenix, the TRC can potentially save 86.3 MJ·m<sup>-2</sup> per year. Similar calculations are performed for major cities worldwide [Fig. 4(f)]. All locations can benefit from the use of TRC as window coatings to reduce cooling energy.

#### 2.4. Bandpass Filters for TPVs

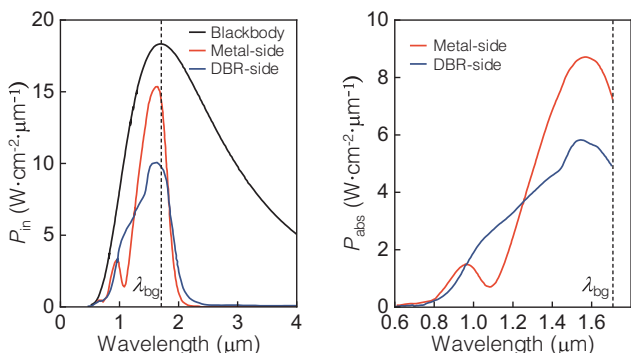
Light-matter interactions in nanophotonic structures at infrared wavelengths have attracted increasing interest

due to their wide-ranging potential applications [91–94]. In conventional solar PV systems, only photons with energy exceeding the bandgap of the PV cell are absorbed to generate photocurrent, whereas other energy losses occur due to thermalization and non-absorbed photons. Unlike traditional solar PV systems, TPV systems use engineered selective emitters to focus on narrowband thermal emission [95]. This approach potentially elevates efficiencies up to the Shockley-Queisser threshold by optimizing photon absorption matched with the spectral response of PV cells [96]. Among the various structures proposed for selective emitters, one-dimensional multilayer Tamm plasmon polaritons (TPPs) have demonstrated advantages in terms of scalable manufacturing and adjustable performance [97]. TPPs are surface waves formed at the boundary between a metallic mirror and a DBR with a zero in-plane wavevector, enabling excitation by incident light of which the in-plane wavevector is less than that of free space [98]. This simple configuration negates the necessity for complex nanostructures to compensate for wavevector mismatch.

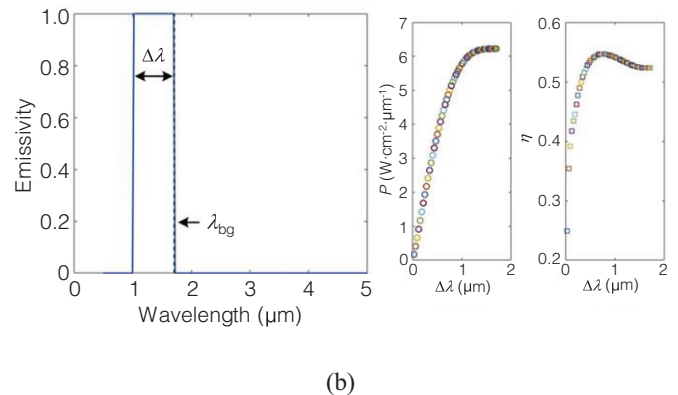
Hu *et al.* [57] conducted research on this design ap-



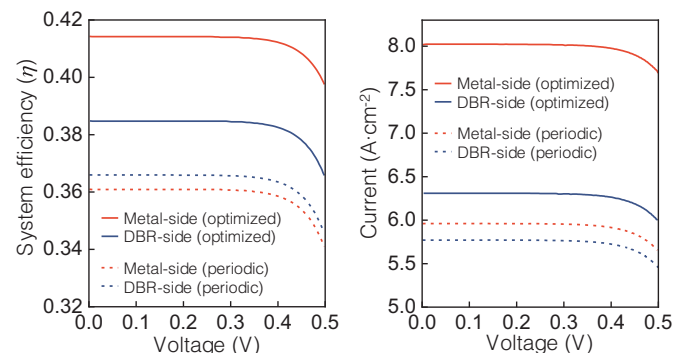
(a)



(c)



(b)



(d)

**FIG. 5.** Simulated results and experimental demonstrations of the designed thermophotovoltaic (TPV) systems. (a) Schematic depicting TPV setups with a metal-side emitter. In the TPV setup, the DBR layer is encoded into binary materials, TiO<sub>2</sub> and SiO<sub>2</sub>, with thicknesses of 30 nm and 51 nm, respectively. The distributed Bragg reflector (DBR)-side emitter shares the same structure, differing only in the position of the SiO<sub>2</sub>/TiO<sub>2</sub> DBR and the W-Al<sub>2</sub>O<sub>3</sub> alloy layer. (b) Ideal emissivity spectrum (left) and the relationship between the unity emissivity bandwidth  $\Delta\lambda$  and power density ( $P$ ) and system efficiency ( $\eta$ ) (right). The system efficiency ( $\eta$ ) peaks at  $\Delta\lambda = 0.696 \mu\text{m}$ . (c) Comparison of incident (left) and absorbed (right) power spectra between metal-side and DBR-side TPV systems. (d) Comparison of system efficiency (left) and photocurrent (right) between optimized and periodic Tamm emitters as a function of voltage. Adapted and modified from Nano Energy 72, Hu *et al.*, article no. 104687. Copyright © 2020, with permission from Elsevier. [57].

proach for TPV systems focusing on optimizing selective emitters to achieve targeted performance. In a typical TPV system [Fig. 5(a)], a high-efficiency absorber captures heat, which is then transferred efficiently to the emitter, maximizing its operating temperature. The emitter is mechanically stabilized by an optically thick refractory material such as tungsten (W), which also acts as a heat spreader for a uniformly high temperature over the emitter. A 10 nm  $\text{Al}_2\text{O}_3$  layer is positioned between the tungsten and the Tamm structure and acts as a spacer. The schematic primarily shows a metal-side emitter, where the metal layer directly faces the PV cell. Alternatively, a DBR-side emitter configuration can be used, where the DBR is oriented toward the PV cell. The DBR structure, which is the focus of the optimization process, consists of alternating layers of  $\text{TiO}_2$  and  $\text{SiO}_2$ , denoted as 0 and 1, with respective bit thicknesses of  $t_0 = 30$  nm for  $\text{TiO}_2$  and  $t_1 = 51$  nm for  $\text{SiO}_2$ . The Tamm emitter directs tailored thermal emission onto the PV cell, where photons with energy greater than the bandgap are absorbed to produce photocurrent, thus generating electricity. The PV cell is kept at a uniform temperature of 300 K using a heat sink.

To design an effective narrow-band selective emitter, both metal-side and DBR-side emitters are optimized using a multilayer design approach based on binary optimization. The Monte Carlo tree search (MCTS) algorithm, combined with Bayesian optimization, is employed to identify the optimal DBR configuration by using a four-step process of selection, expansion, simulation, and backpropagation [99–101]. Each binary sequence of 0s and 1s, from the root to the leaf node, represents a specific configuration of  $\text{TiO}_2$  and  $\text{SiO}_2$  layers in the DBR. Once a DBR configuration is determined, it is integrated into either the metal-side or DBR-side Tamm emitter, after which the corresponding emissivity spectrum, power density, and system efficiency are calculated. The system efficiency ( $\eta$ ) is defined as the ratio of useful power, calculated as absorbed power minus non-radiative losses, to the total incident power. The output from the PV cell model is fed back into the MCTS algorithm for the evaluation and improvement of the current DBR configuration. The objective function of the machine learning-based MCTS algorithm is to maximize both the power density and the system efficiency for metal-side and DBR-side Tamm emitters. The ideal bandwidth for unit emissivity is determined by analyzing the trends of power density and system efficiency as a function of bandwidth ( $\Delta\lambda$ ) [Fig. 5(b)]. As  $\Delta\lambda$  increases, power density ( $P$ ) rises steadily until it reaches a saturation point, whereas system efficiency  $\eta$  peaks at  $\Delta\lambda = 0.696 \mu\text{m}$ . This is because not all absorbed photons generate photocurrent; Excess photon energy is instead converted to heat, which lowers the PV cell's power conversion efficiency. Therefore, the MCTS algorithm targets an emissivity spectrum with unit emissivity over a bandwidth of  $0.696 \mu\text{m}$ , which yields the peak system efficiency.

To compare the performance of the optimized metal-side

and DBR-side emitters, the incident and absorbed power spectra are presented in Fig. 5(c), along with the blackbody irradiance at the same temperature. It is observed that the metal-side emitter exhibits higher intensity near the bandgap wavelength ( $\lambda_{bg}$ ) compared to the DBR-side emitter. The corresponding absorbed power spectra shows absorption exclusively below  $\lambda_{bg}$ , as only photons with energy above this threshold can be effectively absorbed by the PV cell. Additionally, the metal-side emitter demonstrates more efficient power absorption than the DBR-side emitter. Figure 5(d) provides a comparison between the optimized emitter with  $N_{bit} = 15$  for both metal-side and DBR-side configurations and periodically designed emitters with the same  $N_{bit}$ , which serve as a competing model for assessing the machine learning-based designs. When the input voltage increases, both optimized metal-side and DBR-side emitters show superior system efficiency compared to the periodic emitters. Among the optimized emitters, the metal-side emitter exhibits a higher system efficiency, achieving system efficiency  $\eta$  of 0.41 at 0 V. In terms of the generated photocurrent, both MCTS-optimized emitters outperform the periodic emitters, and the metal-side emitter shows superior performance by achieving a photocurrent of  $7.9 \text{ A}\cdot\text{cm}^{-2}$  at 0 V. These results indicate that the periodic DBR structures are limited in performance, whereas the aperiodic DBR structures optimized by MCTS demonstrate the effectiveness of this method in designing selective emitters.

Another study on designing narrow-bandpass filters was conducted by Sakurai *et al.* [58] using Bayesian optimization. Traditionally, thermal emission control has been demonstrated using Fabry–Perot resonators with DBRs [102]. However, these analytical, periodic structures are merely a small subset of the general multilayer configurations. As a result, aperiodic and non-intuitive structures can further enhance performance due to their ability to explore a much larger parametric space compared to conventional designs. Figure 6(a) illustrates the schematic of the design method, where candidate materials Ge, Si, and  $\text{SiO}_2$  are encoded as 1, 2, and 3, respectively, with a tungsten substrate. Each bit thickness is uniformly set, and the number of bits ( $N_{bit}$ ) is fixed at 18. The total thickness  $t_{tot}$  varies from 3.6 to  $4.0 \mu\text{m}$  in increments of  $0.02 \mu\text{m}$ . The objective function aims for unit emissivity at a target wavelength ( $\lambda_t$ ) with a specific bandwidth ( $\Delta\lambda$ ), while minimizing emissivity at other wavelengths within the range ( $\lambda_{min}$  to  $\lambda_{max}$ ) to reduce heat loss, as shown in Fig. 6(b). Bayesian optimization is employed as the machine learning model to predict the surrogate function that searches for the design closest to the target spectrum. Initially, a filter design with  $\lambda_t = 6.0 \mu\text{m}$ ,  $\Delta\lambda = 4.0 \text{ nm}$ ,  $\lambda_{min} = 4.0 \mu\text{m}$ , and  $\lambda_{max} = 8.0 \mu\text{m}$  is optimized. The result is a multilayer containing only Ge and  $\text{SiO}_2$  with a total thickness of  $t_{tot} = 3.80 \mu\text{m}$ . Two additional designs are optimized under similar conditions, targeting  $\lambda_t$  values of  $5.0 \mu\text{m}$  and  $7.0 \mu\text{m}$ . Based on the initial results, Ge and  $\text{SiO}_2$  are selected as the material bases for these subsequent optimizations. Figure 6(c) compares the simulated and

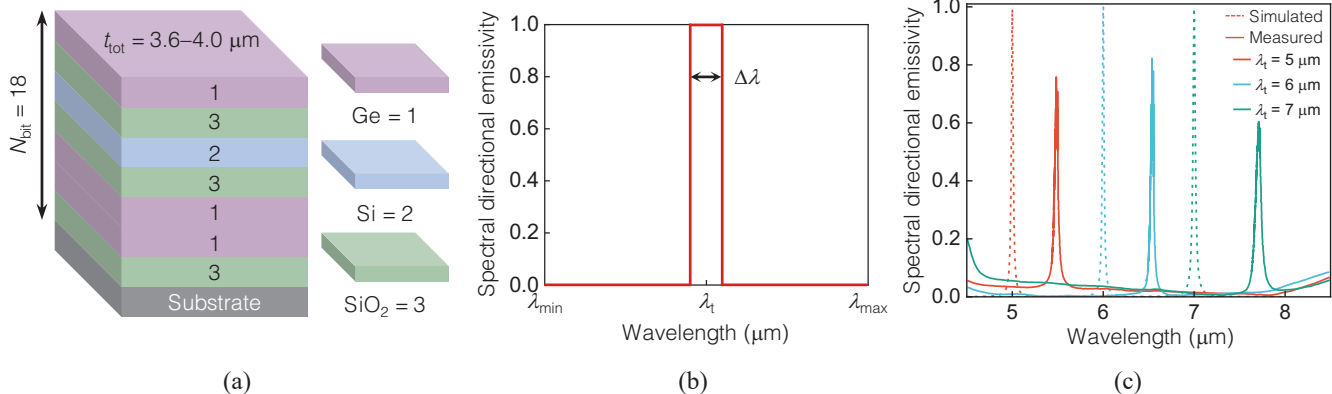


**FIG. 6.** Simulated and measured emissivity spectra of narrow-bandpass filters designed through Bayesian optimization. (a) Schematic illustrating the design of a narrow-bandpass filter. Three materials ( $\text{Ge}$ ,  $\text{Si}$ , and  $\text{SiO}_2$ ) are used to make the filter, and the thickness of each layer is evenly distributed. The number of bits is fixed at 18, and the total filter thickness varies from  $3.6 \mu\text{m}$  to  $4.0 \mu\text{m}$ . (b) Ideal spectral directional emissivity spectrum of the filter. The ideal spectrum exhibits sharp unit emissivity at the target wavelength  $\lambda_t$  with a bandwidth  $\Delta\lambda$ , while the emissivity is zero across the rest of the spectrum, from  $\lambda_{\text{min}}$  to  $\lambda_{\text{max}}$ . (c) The simulated (dashed lines) and measured (solid lines) spectral directional emissivity of the fabricated structures, designed for target wavelengths ( $\lambda_t$ ) of  $5.0 \mu\text{m}$  (red),  $6.0 \mu\text{m}$  (blue), and  $7.0 \mu\text{m}$  (green). Adapted and modified from Sakurai *et al.*, ACS Cent. Sci. 2019; **5**; 319–326. Copyright © 2019, American Chemical Society [58]. This is an unofficial adaptation of an article that appeared in an ACS publication. ACS has not endorsed the content of this adaptation or the context of its use.

measured emissivity spectra. The optimized emissivity spectra (dashed lines) for  $\lambda_t = 5.0 \mu\text{m}$ ,  $6.0 \mu\text{m}$ , and  $7.0 \mu\text{m}$  exhibit sharp, high emissivity with  $Q$ -factors of 217, 273, and 233, respectively. The measured emissivity spectra of the fabricated samples are shown as solid lines, showing a peak wavelength shift of approximately  $0.5 \mu\text{m}$ , with peak emissivity of 0.76, 0.83, and 0.61, and  $Q$ -factors of 132, 188, and 109, respectively. The discrepancy between the peak positions is attributed to fabrication errors, particularly deviations in deposited thickness compared to the simulated structures. Despite these discrepancies, the machine learning optimization approach demonstrates improved emissivity and  $Q$ -factor values compared to conventional narrow-bandpass filters, highlighting the advantages of aperiodic multilayers.

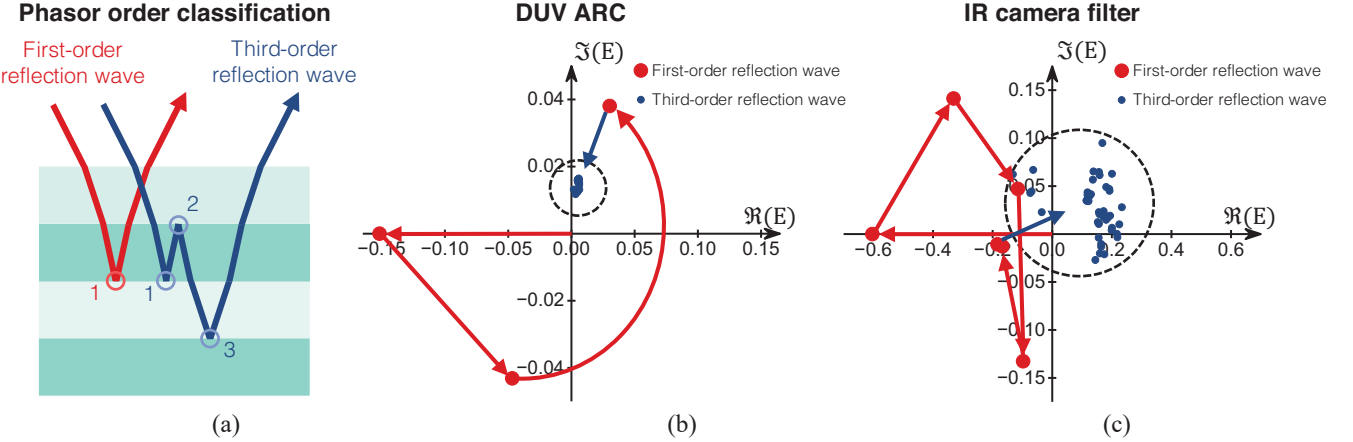
### III. CONCLUSION

In summary, we review three practical applications where binary-optimization-based multilayer designs effectively achieve optical performance close to the target spectra. Binary optimization enables the design of complex multilayers that meet requirements that are unattainable with conventional analytical methods. Encoding the continuous system into a reduced binary space saves significant computational efforts without compromising accuracy. Additionally, unlike more resource-intensive platforms such as neural networks, the FM model used for QUBO problems reveals the underlying physics of aperiodic or non-intuitive multilayers. For instance, ARCs depend on the interaction between adjacent layers, where the reflectance is influenced by each layer's refractive index and thickness. The FM model's approach to predicting pairwise interactions successfully interprets these layer-to-layer dynamics to analyze

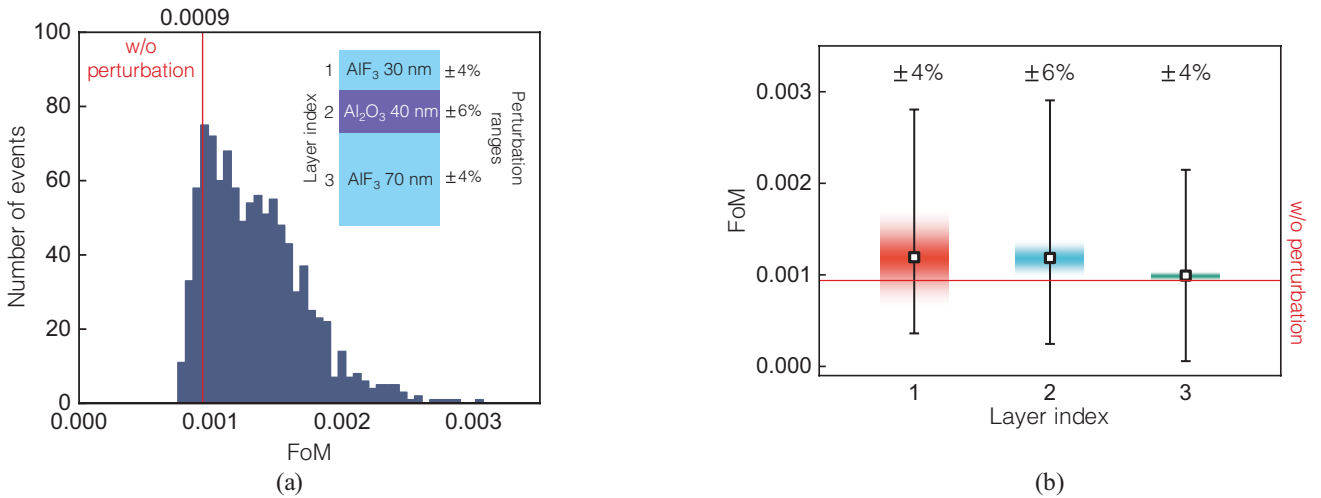
overall antireflective performance. However, relying solely on pairwise interactions may limit the capacity of the model to represent complex systems. For more complex systems, the development of a higher-order machine learning model that considers interactions beyond simple pairwise relationships is necessary.

Figure 7(a) illustrates a schematic for classifying phasors by reflection order. The first-order reflection wave includes phasors resulting from a single reflection, while the third-order reflection wave includes those from three reflections. Note that only odd-numbered reflections are considered. Figures 7(b) and 7(c) display phasor diagrams for a DUV ARC and an IR camera filter. In the DUV ARC, which targets a single wavelength, a clear phasor convergence is observed as third-order reflection waves are added to first-order reflections. This indicates that the pairwise interaction of the FM model is well-suited to the design of the given system. In contrast, the IR camera filter, designed for a broader spectral range ( $8\text{--}13 \mu\text{m}$ ), shows more dispersed phasors even with third-order reflections, suggesting the need for a higher-order machine learning model to interpret such complex interactions effectively.

Another perspective in binary-optimization-based multilayer design can involve enhancing fabrication fidelity. Defining the FoM equation solely based on optical properties does not account for practical fabrication constraints, such as achievable deposition thickness, potential deposition errors influenced by layer height, or refractive index shifts in ultrathin layers compared to bulk materials. A statistical approach to analyzing the tolerance of designed structures to thickness errors can help address potential fabrication discrepancies. In Fig. 8(a), we illustrate FoM distribution by randomly perturbing all layers within a specified range for the triple-layer DUV ARC design, with the original FoM



**FIG. 7.** Comparative analysis of phasor diagrams between deep ultraviolet antireflective coating (DUV ARC) and infrared (IR) camera coating. (a) Phasor order classification for incident light experiencing multiple reflections inside the multilayer. The red-colored light path indicates the first-order reflection wave, corresponding to one reflection. The blue-colored light path indicates the third-order reflection wave, corresponding to three reflections. (b) Phasor diagram of a DUV ARC optimized using an AlF<sub>3</sub>/Al<sub>2</sub>O<sub>3</sub> triple-layer, with a total thickness of 180 nm. Red points represent the sequentially added phasors of the first-order reflection waves, while blue points represent the resultant phasors after considering third-order reflection waves, following the addition of all possible first-order reflection waves. (c) Phasor diagram of an IR camera filter composed of five Ge/YF<sub>3</sub> layers, with a total thickness of 2,400 nm.



**FIG. 8.** Analysis of figure-of-merit (FoM) deviations under random perturbations. (a) Distribution graph of the FoM versus random perturbations applied to an optimized deep ultraviolet antireflective coating (DUV ARC). Random perturbations, within a user-defined range, were applied 1,000 times across all physical layers. The red line indicates the FoM without any perturbation. The inset shows the structure of an optimized triple-layer DUV ARC with user-defined perturbation ranges for each layer. (b) Column graph showing the standard deviation of 1,000 random perturbations applied to each individual physical layer, represented by the layer index. The red, blue, and green bars indicate the standard deviation and the black squares indicate the mean values, and error bars show the minimum and maximum FoM values.

indicated by a red line. By applying 1,000 random perturbations, we assess tolerance by measuring FoM deviation from its original value. This analysis can also be applied to individual layers, as shown in Fig. 8(b), where the black squares indicate mean FoM values, and error bars represent the maximum and minimum FoM values after perturbation. The incorporation of fabrication fidelity into the FoM allows for a multilayer design that remains robust under realistic fabrication conditions. In addition, cost optimization is feasible by applying penalties for layer increases,

which encourages high-performing structures with fewer physical layers. In conclusion, binary-optimization-based multilayer design offers a versatile approach for creating high-performance optical structures, efficiently balancing computational time, performance, and fabrication requirements, all achievable with precise formulation of the FoM equation.

## FUNDING

This work was supported by the Hyundai-NGV Program (Grant No. R232604.0003) and the National Research Foundation (NRF) of Korea through the Basic Science Research Program (Grant No. RS-2023-00207966).

## DISCLOSURES

The authors declare that they have no known competing financial interests or personal relationships that could have appeared to influence the work reported in this paper.

## DATA AVAILABILITY

Data sharing is not applicable to this article since no new data were created or analyzed in this study.

## REFERENCES

1. A. Piegari and F. Flory, *Optical Thin Films and Coatings: From Materials to Applications*, 2<sup>nd</sup> ed. (Woodhead Publishing, UK, 2018).
2. P. Dhez and C. Weisbuch, *Physics, fabrication, and applications of multilayered structures*, 1<sup>st</sup> ed. (Springer Science & Business Media, Germany, 2013).
3. S. Laux, K. Mann, B. Granitza, U. Kaiser, and W. Richter, “Antireflection coatings for UV radiation obtained by molecular-beam deposition,” *Appl. Opt.* **35**, 6216–6218 (1996).
4. E. T. Hamden, A. D. Jewell, C. A. Shapiro, S. R. Cheng, T. M. Goodsall, J. Hennessy, M. Hoenk, T. Jones, S. Gordon, H. R. Ong, D. Schiminovich, D. C. Martin, and S. Nikzad, “Charge-coupled devices detectors with high quantum efficiency at UV wavelengths,” *J. Astron. Telesc. Instrum. Syst.* **2**, 036003 (2016).
5. C. Liu, M. Kong, and B. Li, “Performance optimization of 193 nm antireflective coatings with wide incident angle ranges on strongly curved spherical substrates,” *Opt. Express* **26**, 19524–19533 (2018).
6. M. J. Cangemi, P. G. Dewa, J. D. Malach, P. F. Michaloski, H. Schreiber, and J. Wang, “Silica-modified-fluoride broad angle anti-reflection coatings,” U.S. Patent US9482790B2 (2016).
7. M. Dandin, P. Abshire, and E. Smela, “Optical filtering technologies for integrated fluorescence sensors,” *Lab Chip* **7**, 955–977 (2007).
8. K.-T. Lee, S.Y. Seo, J. Y. Lee, and L. J. Guo, “Strong resonance effect in a lossy medium-based optical cavity for angle robust spectrum filters,” *Adv. Mater.* **26**, 6324–6328 (2014).
9. S. A. Kumar, C. L. Nagendra, H. G. Shanbhogue, and G. K. M. Thutupalli, “Near-infrared bandpass filters from Si/SiO<sub>2</sub> multilayer coatings,” *Opt. Eng.* **38**, 368–380 (1999).
10. W. Withayachumnankul, B. M. Fischer, and D. Abbott, “Quarter-wavelength multilayer interference filter for terahertz waves,” *Opt. Commun.* **281**, 2374–2379 (2008).
11. P. M. Kaminski, F. Lisco, and J. M. Walls, “Multilayer broadband antireflective coatings for more efficient thin film CdTe solar cells,” *IEEE J. Photovolt.* **4**, 452–456 (2014).
12. J. H. Selj, T. T. Mongstad, R. Søndenå, and E. S. Marstein, “Reduction of optical losses in colored solar cells with multilayer antireflection coatings,” *Sol. Energy Mater. Sol. Cells* **95**, 2576–2582 (2011).
13. W. Zhang, K. Hu, J. Tu, A. Aierken, D. Xu, G. Song, X. Sun, L. Li, K. Chen, and D. Zhang, “Broadband graded refractive index TiO<sub>2</sub>/Al<sub>2</sub>O<sub>3</sub>/MgF<sub>2</sub> multilayer antireflection coating for high efficiency multi-junction solar cell,” *Sol. Energy* **217**, 271–279 (2021).
14. S. Saylan, T. Milakovich, S. A. Hadi, A. Nayfeh, E. A. Fitzgerald, and M. S. Dahlem, “Multilayer antireflection coating design for GaAs<sub>0.69</sub>P<sub>0.31</sub>/Si dual-junction solar cells,” *Sol. Energy* **122**, 76–86 (2015).
15. B. G. Priyadarshini and A. K. Sharma, “Design of multi-layer anti-reflection coating for terrestrial solar panel glass,” *Bull. Mater. Sci.* **39**, 683–689 (2016).
16. G. K. Dalapati, A. K. Kushwaha, M. Sharma, V. Suresh, S. Shannigrahi, S. Zhuk, and S. Masudy-Panah, “Transparent heat regulating (THR) materials and coatings for energy saving window applications: Impact of materials design, microstructural, and interface quality on the THR performance,” *Prog. Mater. Sci.* **95**, 42–131 (2018).
17. L. Yao, Z. Qu, R. Sun, Z. Pang, Y. Wang, B. Jin, and J. He, “Long-lived multilayer coatings for smart windows: Integration of energy-saving, antifogging, and self-healing functions,” *ACS Appl. Energy Mater.* **2**, 7467–7473 (2019).
18. K. Han and J. H. Kim, “Reflectance modulation of transparent multilayer thin films for energy efficient window applications,” *Mater. Lett.* **65**, 2466–2469 (2011).
19. A. A. Solovyev, S. V. Rabotkin, and N. F. Kovsharov, “Polymer films with multilayer low-E coatings,” *Mater. Sci. Semicond. Process.* **38**, 373–380 (2015).
20. J. Kim, S. Baek, J. Y. Park, K. H. Kim, and J.-L. Lee, “Photonic multilayer structure induced high near-infrared (NIR) blockage as energy-saving window,” *Small* **17**, 2100654 (2021).
21. O. Razskazovskaya, F. Krausz, and V. Pervak, “Multilayer coatings for femto-and attosecond technology,” *Optica* **4**, 129–138 (2017).
22. G. Emiliani, A. Piegari, S. D. Silvestri, P. Laporta, and V. Magni, “Optical coatings with variable reflectance for laser mirrors,” *Appl. Opt.* **28**, 2832–2837 (1989).
23. M. Zhu, N. Xu, B. Roshanzadeh, S. T. P. Boyd, W. Rudolph, Y. Chai, and J. Shao, “Nanolaminate-based design for UV laser mirror coatings,” *Light Sci. Appl.* **9**, 20 (2020).
24. D. R. Gibson, I. Brinkley, and J. M. Walls, “Optical coatings and thin films for display technologies using closed field magnetron sputtering,” *Proc. SPIE* **5618**, 578435 (2004).
25. A. Genco, G. Giordano, S. Carallo, G. Accorsi, Y. Duan, S. Gambino, and M. Mazzeo, “High quality factor microcavity OLED employing metal-free electrically active Bragg mirrors,” *Org. Electron.* **62**, 174–180 (2018).
26. P.-H. Lei, S.-H. Wang, F. S. Juang, Y.-H. Tseng, and M.-J. Chung, “Effect of SiO<sub>2</sub>/Si<sub>3</sub>N<sub>4</sub> dielectric distributed Bragg re-

- flectors (DDBRs) for Alq<sub>3</sub>/NPB thin-film resonant cavity organic light emitting diodes," *Opt. Commun.* **283**, 1933–1937 (2010).
27. M. Chakaroun, A. T. Diallo, S. Hamdad, S. Kadir, A. P. A. Fischer, and A. Boudrioua, "Experimental and theoretical study of the optical properties optimization of an OLED in a microcavity," *IEEE Trans. Electron Devices* **65**, 4897–4904 (2018).
28. J. T. Cox, G. Hass, and A. Thelen, "Triple-layer antireflection coatings on glass for the visible and near infrared," *J. Opt. Soc. Am* **52**, 965–969 (1962).
29. C. L. Nagendra and G. K. M. Thutupalli, "Design of three-layer antireflection coatings: A generalized approach," *Appl. Opt.* **27**, 2320–2333 (1988).
30. N. Kaiser and H. K. Pulker, *Optical Interference Coatings*, 1<sup>st</sup> ed. (Springer Berlin, Germany, 2013).
31. M. Kim, D. Lee, S. Son, Y. Yang, H. Lee, and J. Rho, "Visibly transparent radiative cooler under direct sunlight," *Adv. Opt. Mat.* **9**, 2002226 (2021).
32. M. M. Hossain and M. Gu, "Radiative cooling: Principles, progress, and potentials," *Adv. Sci.* **3**, 1500360 (2016).
33. H. Zhang, Z. Huang, M. Ding, Q. Wang, Y. Feng, Z. Li, S. Wang, L. Yang, S. Chen, W. Shang, J. Zhang, T. Deng, H. Xu, and K. Cui, "A photon-recycling incandescent lighting device," *Sci. Adv.* **9**, eadf3737 (2023).
34. L. Frey, P. Parrein, J. Raby, C. Pellé, D. Hérault, M. Marty, and J. Michailos, "Color filters including infrared cut-off integrated on CMOS image sensor," *Opt. Express* **19**, 13073–13080 (2011).
35. A. V. Tikhonravov, M. K. Trubetskoy, and G. W. DeBell, "Application of the needle optimization technique to the design of optical coatings," *Appl. Opt.* **35**, 5493–5508 (1996).
36. A. V. Tikhonravov, "Some theoretical aspects of thin-film optics and their applications," *Appl. Opt.* **32**, 5417–5426 (1993).
37. A. V. Tikhonravov, "Optimality of thin film optical coating design," *Proc. SPIE* **1270**, 119899 (1990).
38. S. Larouche and L. Martinu, "OpenFilters: Open-source software for the design, optimization, and synthesis of optical filters," *Appl. Opt.* **47**, C219–C230 (2008).
39. Y. Shi, W. Li, A. Raman, and S. Fan, "Optimization of multilayer optical films with a memetic algorithm and mixed integer programming," *ACS Photonics* **5**, 684–691 (2017).
40. W. Li, Y. Shi, Z. Chen, and S. Fan, "Photonic thermal management of coloured objects," *Nat. Commun.* **9**, 4240 (2018).
41. F. Neri and C. Cotta, "Memetic algorithms and memetic computing optimization: A literature review," *Swarm Evol. Comput.* **2**, 1–14 (2012).
42. S. J. Patel and V. Kheraj, "Optimization of the genetic operators and algorithm parameters for the design of a multilayer anti-reflection coating using the genetic algorithm," *Opt. Laser Technol.* **70**, 94–99 (2015).
43. J. Jiang, J. Cai, G. P. Nordin, and L. Li, "Parallel microgenetic algorithm design for photonic crystal and waveguide structures," *Opt. Lett.* **28**, 2381–2383 (2003).
44. L. Sanchis, A. Håkansson, D. López-Zanón, J. Bravo-Abad, and J. Sánchez-Dehesa, "Integrated optical devices design by genetic algorithm," *Appl. Phys. Lett.* **84**, 4460–4462 (2004).
45. S. So, Y. Yang, S. Son, D. Lee, D. Chae, H. Lee, and J. Rho, "Highly suppressed solar absorption in a daytime radiative cooler designed by genetic algorithm," *Nanophotonics* **11**, 2107–2115 (2022).
46. K. Shimazaki, A. Ohnishi, and Y. Nagasaka, "Development of spectral selective multilayer film for a variable emittance device and its radiation properties measurements," *Int. J. Thermophys.* **24**, 757–769 (2003).
47. A. Sakurai, H. Tanikawa, and M. Yamada, "Computational design for a wide-angle cermet-based solar selective absorber for high temperature applications," *J. Quant. Spectrosc. Radiat.* **132**, 80–89 (2014).
48. J. Peurifoy, Y. Shen, L. Jing, Y. Yang, F. Cano-Renteria, B. G. DeLacy, J. D. Joannopoulos, M. Tegmark, and M. Soljačić, "Nanophotonic particle simulation and inverse design using artificial neural networks," *Sci. Adv.* **4**, eaar4206 (2018).
49. D. Liu, Y. Tan, E. Khoram, and Z. Yu, "Training deep neural networks for the inverse design of nanophotonic structures," *ACS Photonics* **5**, 1365–1369 (2018).
50. O. Yesilyurt, S. Peana, V. Mkhitaryan, K. Pagadala, V. M. Shalaev, A. V. Kildishev, and A. Boltasseva, "Fabrication-conscious neural network based inverse design of single-material variable-index multilayer films," *Nanophotonics* **12**, 993–1006 (2023).
51. H. Wang, Z. Zheng, C. Ji, and L. J. Guo, "Automated multi-layer optical design via deep reinforcement learning," *Mach. Learn.: Sci. Technol.* **2**, 025013 (2021).
52. S. So, T. Badloe, J. Noh, J. Bravo-Abad, and J. Rho, "Deep learning enabled inverse design in nanophotonics," *Nanophotonics* **9**, 1041–1057 (2020).
53. B. A. Wilson, Z. A. Kudyshev, A. V. Kildishev, S. Kais, V. M. Shalaev, and A. Boltasseva, "Machine learning framework for quantum sampling of highly constrained, continuous optimization problems," *Appl. Phys. Rev.* **8**, 041418 (2021).
54. J.-H. Kim, D. I. Kim, S. S. Lee, K.-S. An, S. Yim, E. Lee, and S.-K. Kim, "Wide-angle deep ultraviolet antireflective multilayers via discrete-to-continuous optimization," *Nanophotonics* **12**, 1913–1921 (2023).
55. G.-T. Park, J.-H. Kim, S. Lee, D. I. Kim, K.-S. An, E. Lee, S. Yim, and S.-K. Kim, "Conformal antireflective multilayers for high-numerical-aperture deep-ultraviolet lenses," *Adv. Opt. Mater.* **12**, 2401040 (2024).
56. S. Kim, W. Shang, S. Moon, T. Pastega, E. Lee, and T. Luo, "High-performance transparent radiative cooler designed by quantum computing," *ACS Energy Lett.* **7**, 4134–4141 (2022).
57. R. Hu, J. Song, Y. Liu, W. Xi, Y. Zhao, X. Yu, Q. Cheng, G. Tao, and X. Luo, "Machine learning-optimized Tamm emitter for high-performance thermophotovoltaic system with detailed balance analysis," *Nano Energy* **72**, 104687 (2020).
58. A. Sakurai, K. Yada, T. Simomura, S. Ju, M. Kashiwagi, H. Okada, T. Nagao, K. Tsuda, and J. Shiomi, "Ultranarrow-band wavelength-selective thermal emission with aperiodic multi-layered metamaterials designed by Bayesian optimization,"

- ACS Cent. Sci. **5**, 319–326 (2019).
59. C. Middleton, “5 things you should know about High NA EUV lithography,” (ASML Holding N.V., Published date: Jan. 25, 2024), <https://www.asml.com/en/news/stories/2024/5-things-high-na-euv> (Accessed date: Oct. 22, 2024).
60. C. Zahlten, P. Gräupner, J. Schoot, P. Kürz, J. Stoeldraijer, and W. Kaiser, “High-NA EUV lithography: Pushing the limits,” Proc. SPIE **11177**, 111770B (2019).
61. D. L. Goldfarb, W. Broadbent, M. Wylie, N. Felix, and D. Corliss, “Through-pellicle defect inspection of EUV masks using an ArF-based inspection tool,” Proc. SPIE **9776**, 97761H (2016).
62. N. G. Orji, M. Badaroglu, B. M. Barnes, C. Beitia, B. D. Bunday, U. Celano, R. J. Kline, M. Neisser, Y. Obeng, and A. E. Vladar, “Metrology for the next generation of semiconductor devices,” Nat. Electron. **1**, 532–547 (2018).
63. J. Zhang, Y. Kim, Y. Kim, R. Valencia, T. D. Milster, and D. Dozer, “High resolution semiconductor inspection by using solid immersion lenses,” Jpn. J. Appl. Phys. **48**, 03A043 (2009).
64. M. Rothschild, “A roadmap for optical lithography,” Opt. Photonics News **21**, 26–31 (2010).
65. T. Ito and S. Okazaki, “Pushing the limits of lithography,” Nature **406**, 1027–1031 (2000).
66. S. V. Sreenivasan, “Nanoimprint lithography steppers for volume fabrication of leading-edge semiconductor integrated circuits,” Microsyst. Nanoeng. **3**, 17075 (2017).
67. R. D. Shannon, R. C. Shannon, O. Medenbach, and R. X. Fischer, “Refractive index and dispersion of fluorides and oxides,” J. Phys. Chem. Ref. Data **31**, 931–970 (2002).
68. T. Yoshida, K. Nishimoto, K. Sekine, and K. Etoh, “Fluoride antireflection coatings for deep ultraviolet optics deposited by ion-beam sputtering,” Appl. Opt. **45**, 1375–1379 (2006).
69. L. Bin-Cheng, L. Da-Wei, H. Yan-Ling, G. Chun, Z. Yun-Dong, and L. Hong-Xiang, “Anti-reflective fluoride coatings for widely tunable deep-ultraviolet diode-pumped solid-state laser applications,” Chin. Phys. Lett. **27**, 044201 (2010).
70. D. Ristau, S. Günster, S. Bosch, A. Duparre, E. Masetti, J. Ferre-Borrull, G. Kiriakidis, F. Peiro, E. Quesnel, and A. Tikhonravov, “Ultraviolet optical and microstructural properties of MgF<sub>2</sub> and LaF<sub>3</sub> coatings deposited by ion-beam sputtering and boat and electron-beam evaporation,” Appl. Opt. **41**, 3196–3204 (2002).
71. D. Ehrt, “Deep-UV materials,” Adv. Opt. Technol. **7**, 225–242 (2018).
72. S. Rendle, “Factorization machines,” in *Proc. IEEE International Conference on Data Mining* (Sydney, Australia, Dec. 13–17, 2010), pp. 995–1000.
73. J. P. Hannon, N. V. Hung, G. T. Trammell, E. Gerdau, M. Mueller, R. Rüffer, and H. Winkler, “Grazing-incidence antireflection films. II. Alternate techniques and general multi-layer theory,” Phys. Rev. B **32**, 5081 (1985).
74. M. A. Kats, D. Sharma, J. Lin, P. Genevet, R. Blanchard, Z. Yang, M. M. Qazilbash, D. N. Basov, S. Ramanathan, and F. Capasso, “Ultra-thin perfect absorber employing a tunable phase change material,” Appl. Phys. Lett. **101**, 221101 (2012).
75. X.-L. Zhang, J.-F. Song, X.-B. Li, J. Feng, and H.-B. Sun, “Anti-reflection resonance in distributed Bragg reflectors-based ultrathin highly absorbing dielectric and its application in solar cells,” Appl. Phys. Lett. **102**, 103901 (2013).
76. E. A. Goldstein, A. P. Raman, and S. Fan, “Sub-ambient non-evaporative fluid cooling with the sky,” Nat. Energy **2**, 17143 (2017).
77. B. Zhu, W. Li, Q. Zhang, D. Li, X. Liu, Y. Wang, N. Xu, Z. Wu, J. Li, and X. Li, “Subambient daytime radiative cooling textile based on nanoprocessed silk,” Nat. Nanotechnol. **16**, 1342–1348 (2021).
78. A. P. Raman, M. A. Anoma, L. Zhu, E. Rephaeli, and S. Fan, “Passive radiative cooling below ambient air temperature under direct sunlight,” Nature **515**, 540–544 (2014).
79. Z. Chen, L. Zhu, A. Raman, and S. Fan, “Radiative cooling to deep sub-freezing temperatures through a 24-h day–night cycle,” Nat. Commun. **7**, 13729 (2016).
80. Y. Zhai, Y. Ma, S. N. David, D. Zhao, R. Lou, G. Tan, R. Yang, and X. Yin, “Scalable-manufactured randomized glass-polymer hybrid metamaterial for daytime radiative cooling,” Science **355**, 1062–1066 (2017).
81. T. Li, Y. Zhai, S. He, W. Gan, Z. Wei, M. Heidarnejad, D. Dalgo, R. Mi, X. Zhao, and J. Song, J. Dai, C. Chen, A. Aili, A. Vellore, A. Martini, R. Yang, J. Srebric, X. Yin, and L. Hu, “A radiative cooling structural material,” Science **364**, 760–763 (2019).
82. A. Leroy, B. Bhatia, C. C. Kelsall, A. Castillejo-Cuberos, M. Di Capua H., L. Zhao, L. Zhang, A. M. Guzman, and E. N. Wang, “High-performance subambient radiative cooling enabled by optically selective and thermally insulating polyethylene aerogel,” Sci. Adv. **5**, eaat9480 (2019).
83. J. Mandal, M. Jia, A. Overvig, Y. Fu, E. Che, N. Yu, and Y. Yang, “Porous polymers with switchable optical transmittance for optical and thermal regulation,” Joule **3**, 3088–3099 (2019).
84. D. Zhao, A. Aili, Y. Zhai, J. Lu, D. Kidd, G. Tan, X. Yin, and R. Yang, “Subambient cooling of water: Toward real-world applications of daytime radiative cooling,” Joule **3**, 111–123 (2019).
85. X. Xue, M. Qiu, Y. Li, Q. M. Zhang, S. Li, Z. Yang, C. Feng, W. Zhang, J.-G. Dai, and D. Lei, “Creating an eco-friendly building coating with smart subambient radiative cooling,” Adv. Mater. **32**, 1906751 (2020).
86. J.-W. Cho, E.-J. Lee, and S.-K. Kim, “Radiative cooling technologies: A platform for passive heat dissipation,” J. Korean Phys. Soc. **81**, 481–489 (2022).
87. S. Kim, S. Jung, A. Bobbitt, E. Lee, and T. Luo, “Wide-angle spectral filter for energy-saving windows designed by quantum annealing-enhanced active learning,” Cell Rep. Phys. Sci. **5**, 101847 (2024).
88. S. Boixo, T. F. Rønnow, S. V. Isakov, Z. Wang, D. Wecker, D. A. Lidar, J. M. Martinis, and M. Troyer, “Evidence for quantum annealing with more than one hundred qubits,” Nat. Phys. **10**, 218–224 (2014).

89. A. Mishra, T. Albash, and D. A. Lidar, "Finite temperature quantum annealing solving exponentially small gap problem with non-monotonic success probability," *Nat. Commun.* **9**, 2917 (2018).
90. D. Pastorello and E. Blanzieri, "Quantum annealing learning search for solving QUBO problems," *Quantum Inf. Process.* **18**, 303 (2019).
91. S. Fan, "Thermal photonics and energy applications," *Joule* **1**, 264–273 (2017).
92. L. Cui, W. Jeong, V. Fernández-Hurtado, J. Feist, F. J. García-Vidal, J. C. Cuevas, E. Meyhofer, and P. Reddy, "Study of radiative heat transfer in Ångström-and nanometre-sized gaps," *Nat. Commun.* **8**, 14479 (2017).
93. J. C. Cuevas and F. J. García-Vidal, "Radiative heat transfer," *ACS Photonics* **5**, 3896–3915 (2018).
94. Y. Li, X. Bai, T. Yang, H. Luo, and C.-W. Qiu, "Structured thermal surface for radiative camouflage," *Nat. Commun.* **9**, 273 (2018).
95. A. Lenert, D. M. Bierman, Y. Nam, W. R. Chan, I. Celanović, M. Soljačić, and E. N. Wang, "A nanophotonic solar thermophotovoltaic device," *Nat. Nanotechnol.* **9**, 126–130 (2014).
96. O. Dupré, R. Vaillon, and M. A. Green, "Optimization of solar thermophotovoltaic systems including the thermal balance," in *Proc. IEEE 43<sup>rd</sup> Photovoltaic Specialists Conference* (Portland, USA, Jun. 5–10, 2016).
97. M. He, J. R. Nolen, J. Nordlander, A. Cleri, N. S. McIlwaine, Y. Tang, G. Lu, T. G. Folland, B. A. Landman, and J.-P. Maria, "Deterministic inverse design of Tamm plasmon thermal emitters with multi-resonant control," *Nat. Mater.* **20**, 1663–1669 (2021).
98. M. Kaliteevski, I. Iorsh, S. Brand, R. A. Abram, J. M. Chamberlain, A. V. Kavokin, and I. A. Shelykh, "Tamm plasmon-polaritons: Possible electromagnetic states at the interface of a metal and a dielectric Bragg mirror," *Phys. Rev. B* **76**, 165415 (2007).
99. T. M. Dieb, S. Ju, J. Shiomi, and K. Tsuda, "Monte Carlo tree search for materials design and discovery," *MRS Commun.* **9**, 532–536 (2019).
100. S. Ju, T. Shiga, L. Feng, Z. Hou, K. Tsuda, and J. Shiomi, "Designing nanostructures for phonon transport via Bayesian optimization," *Phys. Rev. X* **7**, 021024 (2017).
101. M. Yamawaki, M. Ohnishi, S. Ju, and J. Shiomi, "Multi-functional structural design of graphene thermoelectrics by Bayesian optimization," *Sci. Adv.* **4**, eaar4192 (2018).
102. D. Zhao, L. Meng, H. Gong, X. Chen, Y. Chen, M. Yan, Q. Li, and M. Qiu, "Ultra-narrow-band light dissipation by a stack of lamellar silver and alumina," *Appl. Phys. Lett.* **104**, 221107 (2014).